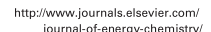


Contents lists available at ScienceDirect

Journal of Energy Chemistry



journal homepage: www.elsevier.com/locate/jechem

Self-assembled synthesis of oxygen-doped g-C₃N₄ nanotubes in enhancement of visible-light photocatalytic hydrogen

Yizeng Zhang a, Zhiwu Chen a,*, Jinliang Li b,*, Zhenya Lu a, Xin Wang a

- ^a School of Materials Science and Engineering, South China University of Technology, Guangzhou 510640, Guangdong, China
- ^b Siyuan Laboratory, Guangdong Provincial Engineering Technology Research Center of Vacuum Coating Technologies and New Energy Materials, Department of Physics, Jinan University, Guangzhou 510632, Guangdong, China

ARTICLE INFO

Article history: Received 13 February 2020 Revised 11 May 2020 Accepted 15 May 2020 Available online 28 May 2020

Keywords: Graphitic carbon nitride Oxygen-doped Nanotube Photocatalytic water splitting Reaction process

ABSTRACT

Currently, photocatalytic water splitting is regarded as promising technology in renewable energy generation. However, the conversion efficiency suffers great restriction due to the rapid recombination of charge carriers. Rational designed the structure and doping elements become important alternative routes to improve the performance of photocatalyst. In this work, we rational designed oxygen-doped graphitic carbon nitride (OCN) nanotubes derived from supermolecular intermediates for photocatalytic water splitting. The as prepared OCN nanotubes exhibit an outstanding hydrogen evolution rate of 73.84 μ mol h⁻¹, outperforming the most of reported one dimensional (1D) g-C₃N₄ previously. Due to the rational oxygen doping, the band structure of g-C₃N₄ is meliorated, which can narrow the band gap and reduce the recombination rate of photogenerated carriers. Furthermore, the hollow nanotube structure of OCN also provide multiple diffuse reflection during photocatalytic reaction, which can significantly promote the utilization capacity of visible light and enhance the photocatalytic water splitting performance. It is believed that our work not only rationally controls the nanostructure, but also introduces useful heteroatom into the matrix of photocatalyst, which provides an effective way to design high-efficiency g-C₃N₄ photocatalyst.

© 2020 Science Press and Dalian Institute of Chemical Physics, Chinese Academy of Sciences. Published by ELSEVIER B.V. and Science Press. All rights reserved.

1. Introduction

The efficient transformation of solar energy into storable, clean and eco-friendly hydrogen via photocatalytic water splitting is identified as one of the most promising way to solve the energy crisis [1–3]. Further developing efficient photocatalysts with abundance and sustainability is urgent [4,5]. As a fascinating polymeric organic semiconductor, graphitic carbon nitride $(g-C_3N_4)$ has attracted a lot of attentions because of its low costs, nontoxicity, strong thermal, chemical stability and special optical features [6–10]. Unfortunately, bulk $g-C_3N_4$ obtained from conventional approaches often present intrinsic drawbacks of small surface area and high photo-generated electron-hole pairs recombination rate, resulting in a poor photocatalytic activity [11–13].

Currently, rational optimizing the nanostructure of photocatalyst is an effective approach to improving the photocatalytic performance of $g-C_3N_4$ [14–16]. Among different nanostructures,

E-mail addresses: chenzw@scut.edu.cn (Z. Chen), lijinliang@email.jnu.edu.cn (J. Li).

nanotube structure of g- C_3N_4 possesses many unique advantages for photocatalytic water splitting, including the multiple diffuse reflection, faster electron transport rate, larger number of active centres and larger specific surface area [17,18]. Currently, the synthetic methods of g- C_3N_4 nanotubes mainly obtain by hard or soft template technologies [19,20]. However, there are many distinct disadvantages for synthesis of nanotube structure by hard template technology, including the complicated process and environmental pollution. Due to the poor structure stability, the soft template technology for synthesis of nanotube structure is immaturity. Therefore, further development of a simple and high-producing technology to obtain g- C_3N_4 nanotubes is urgent.

Some researchers found that the hydrogen bonding has strong directionality and self-assembly of supramolecular precursor by intermolecular hydrogen bonding, which was deemed to an important choice to synthesis of morphologic controllable micro-nano materials [21–23]. Shalom's group synthesized the ordered and hollow g-C₃N₄ using melamine-cyanuric acid complex in ethanol as precursor [24]. Stucky's group obtained 3D macroscopic assemblies of low-dimensional g-C₃N₄ via a similar way by choosing appropriate organic solvents [25]. However, these supramolecular

^{*} Corresponding authors.

precursors are primarily generated via self-assembly between different components in an organic solvent. Compared with organic solvent, water can exhibit more advantageous for self-assembly of molecules by hydrogen bonding, which is helpful to form stable, highly ordered and well-aligned supramolecular precursors. Previously, melamine has been demonstrated that it can be converted to cyanuric acid by hydrolysis at a suitable pH value [26]. This result indicates that the supramolecular precursor can be obtained using melamine by optimization of acidic aqueous solution and we will obtain controllable nanostructure of g-C₃N₄ by the supramolecular precursor.

Currently, element-doping becomes an effective approach to enhance the performance of photocatalysts [27-29]. In all the element-doping, oxygen doping g-C₃N₄ is one of valid approaches for optimizing the electronic and optical performance of g-C₂N₄. which greatly improve its photocatalytic capacity [30–32]. Chen's group developed a facile approach obtained oxygen-doping g-C₃N₄, which could adjust inherent electronic and band structure of the g-C₃N₄, resulting in 2.5 times of hydrogen evolution rate (HER) compared with original g-C₃N₄ [33]. Liu's group synthesized oxygen-doped g-C₃N₄ nanorods by calcination of hydrous melamine nanofibers, which exhibited an excellent visible-light photocatalytic hydrogen evolution of 732 µmol g⁻¹ h⁻¹ [34]. Zhang's group synthesized oxygen substituted g-C₃N₄ via direct annealing method, which operated a promotional photocatalytic hydrogen evolution of 1062.4 μmol h⁻¹ g⁻¹ [35]. Yang's group through fabricated oxygen-doped g-C₃N₄ through thermal polycondensation, which delivered a hydrogen evolution rate of 8.3 mmol h⁻¹ [36]. Despite some works about element-doping in g-C₃N₄ have been reported, their performance still doesn't meet the demand of solar energy conversion. Further developing the nanostructure of g-C₃N₄ with efficient performance become a current research focus for photocatalysis.

In this work, we synthesized oxygen-doped g- C_3N_4 (OCN) nanotubes derived from supermolecular intermediates. According to the observation of the precursor's different reactive state, we obtained formation mechanisms of rod-like supramolecular intermediate and OCN nanotubes. Furthermore, we also found that our OCN nanotubes exhibit tremendous enhancement in light absorption as well as visible-light photocatalytic activity compare with bulk g- C_3N_4 . The optimal OCN nanotube photocatalyst exhibits outstanding HER (73.84 μ mol h⁻¹), which is 6.24 times of bulk g- C_3N_4 . According to the optical and electrical property, the improvement of photocatalytic performance should be owing to the multiple diffuse reflection by the nanotube structure, narrow band gap by the oxygen doping and superior electron transfer capacity. We suggest that our work will provide an effective way to design high-efficiency g- C_3N_4 photocatalyst.

2. Experimental

2.1. Synthesis

The OCN nanotubes are synthesized via a hydrothermal-calcination combined process. Typically, 2 g of melamine was dissolved in 60 mL of deionized water. Then, x g (x = 0, 0.2, 0.4, and 0.6) citric acid were added to the melamine solution. After ultrasonic treatment 1 h and stirring 24 h, the obtained clear solution was poured into a Teflon-lined autoclave and heated to 180 °C for 24 h. After allowing to cool naturally, the products were washed, dried, and the supermolecular intermediates were obtained. The obtained supermolecular intermediates denoted as MCA-x, where x refers to quantity of citric acid used (x = 0, 0.2, 0.4, and 0.6). Afterwards, the supermolecular intermediates were heated to 520 °C for 2 h with a heating rate of 2.2 °C min⁻¹ and

the OCN were obtained. The OCN derived from MCA-x were designated as CN-x, where x refers to quantity of citric acid used (x = 0, 0.2, 0.4, and 0.6). For comparison, bulk g- C_3N_4 (denoted as CN) was obtained by the calcination at 550 °C for 2 h with a heat rate of 2.2 °C min $^{-1}$. For the measurement of Mott-Schottky plots, 20 mg sample and 1 mg polyvinyl alcohol were mixed in water to form slurry. Then the slurry was coated on the graphite paper (2 cm \times 2 cm) and dried at 120 °C over night to obtained the electrode.

2.2. Characterization

The morphologies and structures of our samples were obtained by scanning electron microscopy (SEM, NOVA NANOSEM 430, Netherlands), transmission electron microscope (TEM, JEOL-2100), X-ray diffractometer (XRD, Rigaku D/Max-3C). The surface property was measured by X-ray photoelectron spectroscopy (XPS, Axis uhru DCD) and Fourier transform infrared spectroscopy (FTIR, Perkin Elmer GX). The specific surface areas were determined from the Brunauer-Emmett-Teller (BET) plots. The contents of C and N were determined by CHNSO measurement (Vario EL III elemental analyzer). Solid-state ¹³C MAS nuclear magnetic resonance (NMR) spectra were obtained by a Bruker AVANCE III 400 MHz NMR spectrometer. The photoluminescence emission spectra (PL) were recorded on the PerkinElmer LS55 fluorescence spectrophotometer at 390 nm. The detail measurements of photocurrent and electrochemical impedance spectroscopy (EIS) were described in Supporting Information. The Mott-Schottky plots were obtained by electrochemical workstation (Shanghai Chenhua, CHI 660E) using a three electrodes configuration with a Pt foil as counter electrode and a standard AgCl electrode as reference electrode in 0.1 M Na₂SO₄ aqueous solution.

2.3. Photocatalytic performance measurement

The photocatalysis performances were tested in an on-line photocatalytic analysis system (Labsolar-IIIAG, Beijing Perfectlight, China). Pt (2 wt%) co-catalysts were deposited on the CN or CN-T. Pt deposition was achieved using an in-situ photodeposition method. Briefly, 20 mg photocatalyst powder was dispersed in 80 mL triethanolamine aqueous solution (10 vol%) containing H₂-PtCl₆ (sufficient to achieve a 2 wt% loading). The suspension was then subjected to ultrasonication for 30 min, purged with N2 for 30 min to eliminate O₂ and then sealed. The in-situ photodeposition of Pt was achieved by irradiation with a 500 W mercury lamp (XPA-7 photochemical reactor, Nanjing Xujiang Machine-Electronic Plant) for 1 h. After Pt deposition, the reactor was purged again with N₂ before commencing H₂ production tests. The temperature of the suspension was regulated by an external flow of cold water throughout the photocatalysis. A 300 W Xe lamp equipped with a 420 nm cut-off filter was used as the visible light source for the hydrogen evolution experiments. The quantity of H₂ produced was estimated by a Shimadzu GC-2014 Gas Chromatograph using the average value of five measurements. To explore the reusability, the CN-T photocatalyst was used thrice and the yield of H₂ was measured each time. Following every measurement, the photocatalyst was centrifuged (6000 r min⁻¹), filtered, rinsed, and dried at 100 °C for 3 h.

3. Results and discussion

Fig. 1 shows the SEM images of the pristine melamine and MCA-x. It is found that the melamine displays an irregular shape (Fig. 1 (a)). With the increase of hydrothermal time from 8 h to 24 h, the

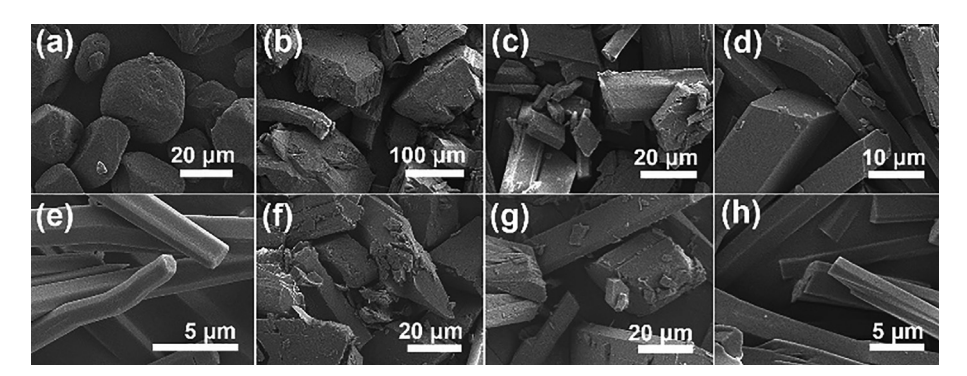


Fig. 1. SEM images of (a) melamine, and the MCA-0.4 after synthesized at 180 °C for (b) 8 h, (c) 16 h, (d) 20 h, (e) 24 h; the SEM images of (f) MCA-0.9, (g) MCA-0.2, (h) MCA-0.6 hydrothermal synthesized at 180 °C for 24 h.

morphology of MCA-0.4 changes gradually from the pristine irregular morphology to the regular rod-like shape. When the hydrothermal time reaches 24 h, the MCA-0.4 possesses a quite regular rod-like morphology with a diameter of about 2-3 μm (Fig. 1(e)). However, with the hydrothermal time further increasing to 28 h, the rod-like intermediate products will fuse and aggregate (Fig. S1), which is due to the destruction of some hydrogen bonds of the supramolecular intermediate. Furthermore, this phenomenon also indicates that the supramolecular intermediate will react with water when the hydrothermal time is extended to 28 h. Fig. 1(e-h) shows the morphologies of supramolecular intermediates with different amount of citric acid in precursor. It is found that the microstructure of the supramolecular intermediate remains an irregular morphology without citric acid, indicating that only a small portion of the melamine is hydrolyzed to cyanuric acid. With the addition of citric acid, all the MCA-x samples display the rod-like shape and their diameter decreases initially and then increases. These results indicate that the synthesis of supramolecular intermediate with rod-like morphology can be easily achieved through modulating hydrothermal time and citric acid quality. Fig. S2(a) shows the XRD patterns of all MCA-x samples. It is found that all the melamines after hydrothermal treatment will form MCA-x. The intensities of the diffraction peaks at 10.93° and 11.95° increase with the increase of citric acid, indicating that citric acid promotes more melamine molecules in-situ hydrolyzed into cyanuric acid, which makes the planar structure more regular. Meanwhile, the XRD pattern of MCA-x is also in accordance with the data reported previously, which can be used as an importance proof for generation of supramolecular intermediate [37]. There are no diffraction peaks of melamine in XRD pattern of MCA-x, indicating that there is essentially no single melamine molecule in the supramolecular intermediates. All melamine molecules are involved in molecular self-assembly and are converted into supramolecular intermediates. However, some weak diffraction peaks of citrate acid were found in the XRD pattern of MCA-x, indicating that some citric acid molecules were adsorbed on supramolecular intermediate's surface. For FTIR spectra in Fig. S2 (b), no significant changes were found between the FTIR spectra of the MCA-x. It is found that the peak at 806 cm⁻¹ ascribed to triazine ring vibration for melamine shift to 780 $\,\mathrm{cm}^{-1}$ for MCA-x after hydrothermal. In addition, a peak at $1707~\text{cm}^{-1}$ for cyanuric acid can be observed, which is attributed to C=O stretching vibration [38,39]. However, it is shifted to 1738 cm⁻¹ for supramolecular intermediate. The shifts of triazine ring vibration to low frequency and the C=O stretching vibration to high frequency for supramolecular intermediate are due to the existence of hydrogen bonding of $N-H \cdot \cdot \cdot N$ and $N-H \cdot \cdot \cdot O$ [40,41]. This result indicates that a portion of melamine is indeed hydrolyzed in situ to cyanuric acid firstly and then the obtained cyanuric acid and remaining melamine will be

immediately combined by hydrogen bonding to form the supramolecular intermediate.

On the basis of above results, the possible synthesis process of MCA-x supramolecular intermediate is proposed, as shown in Fig. 2. Generally, the melamine can be converted to cyanuric acid by hydrolysis at a suitable pH value [26]. Under citric acid assisted hydrothermal conditions, a portion of melamine is hydrolyzed in situ to cyanuric acid accompanied by the escape of NH₃. Then, the obtained cyanuric acid and remaining melamine can be combined via hydrogen bonding, and molecules self-assemble into rod-like supramolecular intermediate. Particularly, three hydrogen bonds are generated between a single melamine molecule and a single cyanuric acid molecule. Citric acid is not involved in the self-assembly process because of its weak reaction with melamine. However, a small amount of citric acid molecules can adsorb on the surface of supramolecular intermediates. During the subsequent heat treatment, oxygen from citric acid can be squeezed into g-C₃N₄ skeletons and oxygen doped g-C₃N₄ can be formed. In conclusion, rod-like MCA-x is successfully synthesized by hydrothermal method just using melamine and citric acid as raw materials, which is a crucial link for the final synthesis of oxygen-doped g-C₃N₄ nanotubes. Meantime, the escaped NH₃ plays an assistant effect on forming of rod-like supramolecular intermediate [42,43].

Fig. 3(a) shows the SEM image of CN, which exhibits the bulk structure. Compared with bulk CN, CN-0.4 derived from supramolecular intermediate exhibits nanotubes structure with a length of 500~800 nm, as shown in Fig. 3(b). From the TEM of CN-0.4 in Fig. 3(e), it is observed that the nanotubes exhibit a diameter of 50~70 nm and a wall thickness of 3~4 nm. Fig. 3(c-f) shows the TEM images of CN-0, CN-0.2 and CN-0.6, respectively. It is observed that the microstructure of the CN-0 remains an irregular morphology, which is originated from the precursor with irregular shape. With the addition of citric acid in precursor solution, both CN-0.2 and CN-0.6 display the nanotube structures, as same as CN-0.4. It is noted that the diameter of the nanotube decreases and then increases with the increase of citric acid in precursor solution, indicating that the suitable citric acid is helpful for the optimization of nanostructure. Such optimization of nanotube structure provides a larger number of active centers and higher visible light absorption-scattering, which can promote the water splitting performance of photocatalyst. Fig. S3 shows the element mapping of OCN-0.4 and it is found that all the elements are distributed uniformly.

Fig. 4(a) shows the XRD patterns of CN, CN-0, CN-0.2, CN-0.4 and CN-0.6. The bulk CN exhibits two peaks at about 13.1° and 27.3°, which are ascribed to in-plane tri-s-triazine units (1 0 0) and inter-planar stacking of conjugated aromatic systems (0 0 2), respectively [44,45]. Compared to bulk CN, the (1 0 0) peak of OCN samples is almost invisible, indicating that the OCN samples

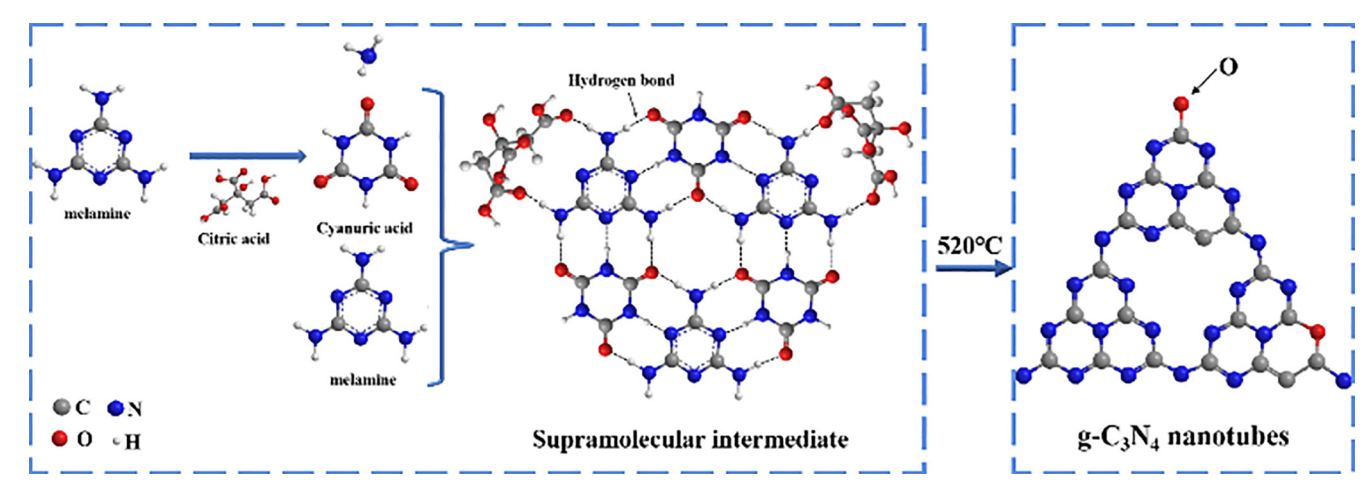


Fig. 2. Formative process of oxygen-doped g-C₃N₄ nanotubes.

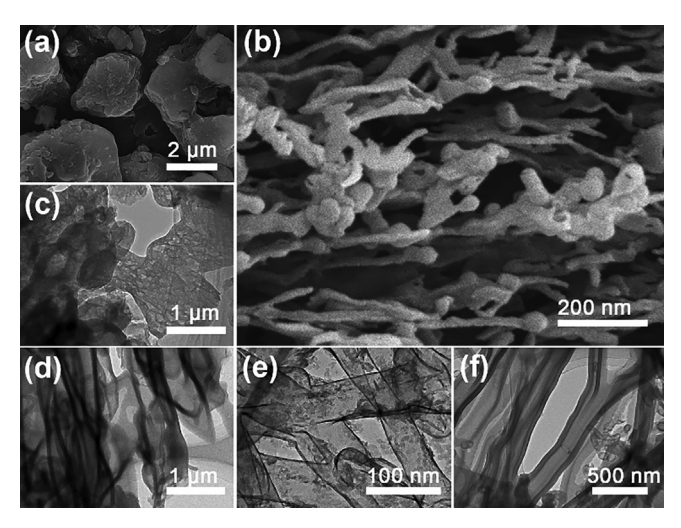


Fig. 3. SEM images of (a) CN and (b) CN-0.4; TEM images of (c) CN-0, (d) CN-0.2, (e) CN-0.4 and (f) CN-0.6.

possess the smaller planar size of the layers [46,47]. Meanwhile, the (0 0 2) peak is broadened and the intensity is weakened, indicating the significant size dependence of g-C₃N₄ nanotubes [37]. However, no other significant change is observed in OCN samples, indicating that all OCN samples have been derived from supramolecular intermediate after heat treatment. Fig. 4(b, c) show the specific surface area and pore size distribution of bulk CN and CN-0.4 nanotubes. Both them exhibit type IV isotherms with Htype hysteresis loops, indicating that both samples are mesoporous structures [48]. According to the calculation by BET method, the specific surface area (SA) of CN-0.4 nanotubes is 52.9 m² g⁻¹, which is 2.29 times of bulk CN (23.1 m^2 g^{-1}). Detailed SAs of all the samples are shown in Table S1. This larger SA can increase the reactive site due to the unique structure of nanotubes, which is in favour of photocatalytic performance. Furthermore, CN-0.4 nanotubes also exhibit more mesoporous compared with CN, which can enhance the diffusion of reactants and products more effectively, thereby improve the reaction kinetics more effectively.

To investigate the defect in the $g-C_3N_4$ nanotubes, the FTIR spectra of CN, CN-0, CN-0.2, CN-0.4 and CN-0.6 are provided in Fig. 4(d). All the samples exhibit three typical main bands of $g-C_3N_4$. An obvious peak at $810~cm^{-1}$ indicates the out-of-plane heptazine bending and the wide band ranging from 3000 to 3400 cm⁻¹ is ascribed to N-H stretching vibration [49]. Some intense peaks in

the range of 1200–1600 cm⁻¹ can be detected, which are related to aromatic skeletal stretching vibrations. It is found that the band of OCN nanotubes between 3000 and 3400 cm⁻¹ is broadened compared with bulk CN, which is due to the O-H stretching vibration [50]. Due to the existence of -OH bond, the hydrophilia of OCN can be promoted, which is helpful to improve its photocatalytic performance. Fig. 4(e) shows the enlarged FTIR spectra of all the samples. It is found that OCN nanotubes show the stretching vibrations at 1236 cm⁻¹, 1317 cm⁻¹ and 1403 cm⁻¹, which are shifted by 7, 9 and 8 cm⁻¹ toward high frequencies compared with bulk CN, respectively. This phenomenon is possibly to the replacement of oxygen atom to nitrogen atom [51]. In addition, compared with bulk CN, an extra weak peak at 1080 cm⁻¹ can be observed, which is corresponding to C-O-C stretching vibration. This result also demonstrates that the oxygen atom has been doped in g-C₃N₄ [51]. To further demonstrate that the oxygen atom has successfully entered into the crystal lattice of g-C₃N₄, solid-state ¹³C magic angle spinning (MAS) NMR of bulk CN and CN-0.4 are provided, as shown in Fig. 4(f). Both samples display two distinct peaks at 157.6 and 165.5 ppm, which are assigned to the C_{3N} (1) and C_{2N-NHx} (2) of heptazines, respectively [45,52]. Compare to bulk CN, two small splits at 158.3 (3) and 166.4 (4) ppm arise in the ¹³C NMR spectra of CN-0.4, indicating that C-O-C bond has been formed, further demonstrating that oxygen atom has been doped in g-C₃N₄ [53].

To investigate the surface structure of samples, the XPS spectra of CN and CN-0.4 are provided. Fig. 5(a) shows the survey XPS spectra of CN and CN-0.4 and both them only exhibit N, O and C peaks without impurity phase. The detail proportion of each atom is shown in Table S2. It is noted that intensity of O 1s peak of CN-0.4 is stronger than that of bulk CN, indicating that CN-0.4 nanotubes exhibit more oxygen atoms on the surface. Fig. 5(b) shows C 1s XPS spectra of bulk CN and CN-0.4. Both samples exhibit three peaks located at 288.2 eV, 286.2 eV, 284.7 eV, which are corresponded to N-C=N, C-NH_x and C-C/C=C, respectively [52]. However, a new peak at 288.9 eV derived from C-O bonds arises in CN-0.4, resulting from the doping oxygen atom into CN heterocycles [54]. Moreover, the peak at 286.2 eV (C-NH_x) of CN-0.4 is weaker than that of bulk CN, which is due to the fact that -NH_x in the CN-0.4 is replaced by -OH. In Fig. 5(c), the N 1s spectra of bulk CN and CN-0.4 can be deconvoluted into three peaks located at 398.7, 400.2, and 401.1 eV, which is ascribed to the twocoordinated C-N=C (N_{2c}), three-coordinated N-C₃ (N_{3c}) and N-H_x group of heptazine framework, respectively [55]. Fig. S4 shows the intensity ratios of N_{2c} and N_{3c} (I_{N2}/I_{N3}) of different samples and it is found that the values of I_{N2}/I_{N3} of samples decease from

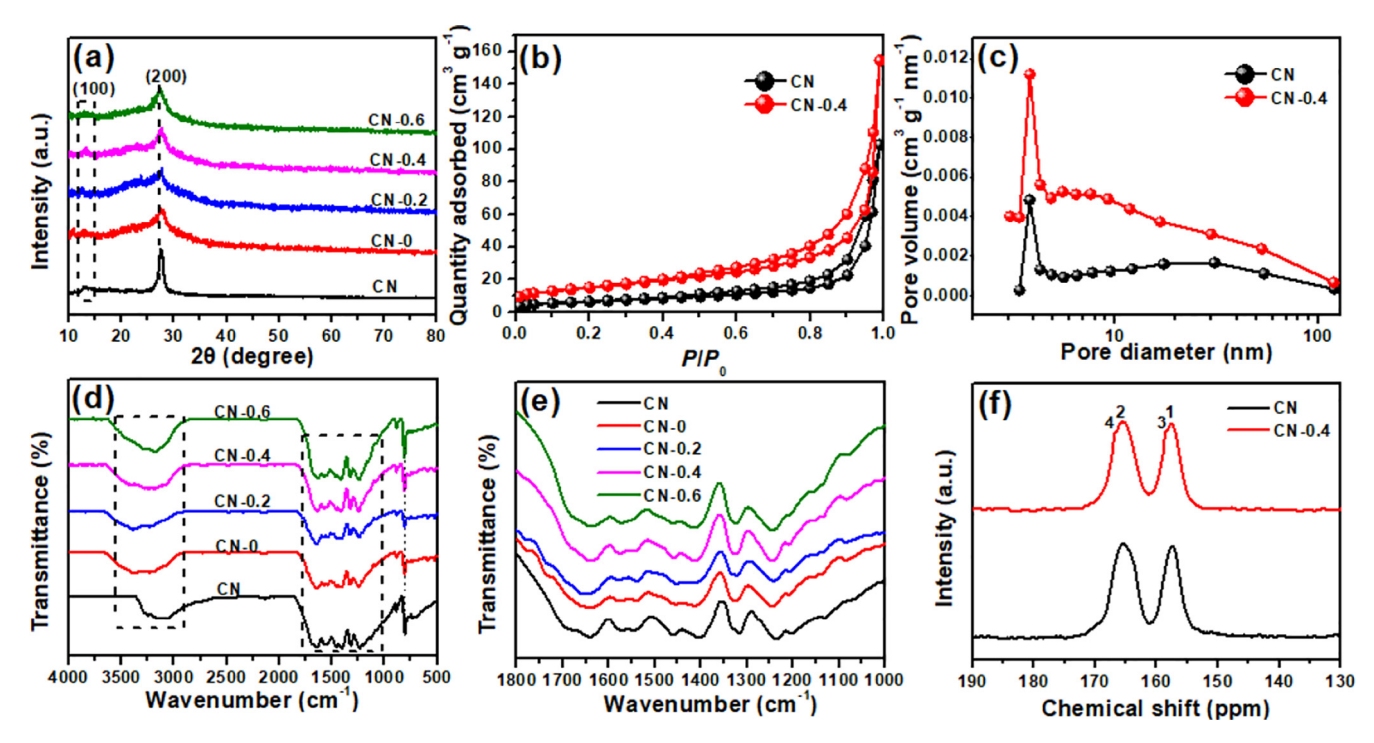


Fig. 4. (a) XRD patterns, (b) nitrogen adsorption—desorption isotherms and (c) corresponding pore size distribution curves of CN and CN-0.4; (d) FTIR spectra and (e) enlarged FTIR spectra of CN, CN-0, CN-0.2, CN-0.4 and CN-0.6, respectively; (f) NMR spectra of CN and CN-0.4.

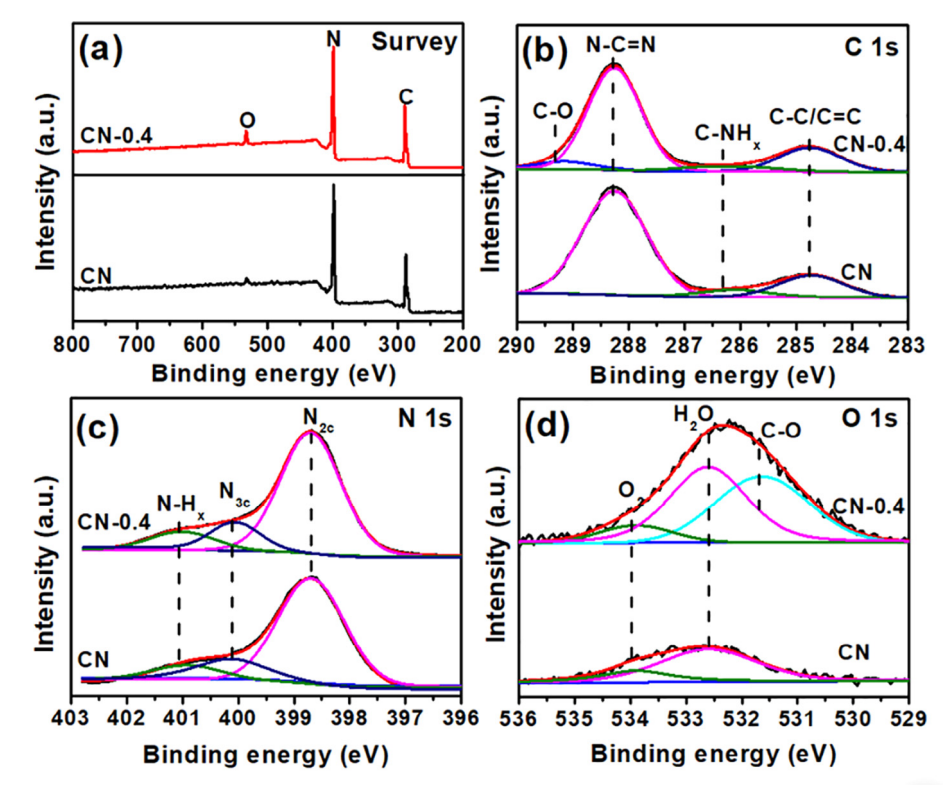


Fig. 5. (a) Survey, (b) C 1s, (c) N 1s and (d) O 1s XPS spectra of CN and CN-0.4.

2.98 (CN) to 2.51 (CN-0.4). This reason is speculated that some two-coordinated (N_{2c}) N atoms in the OCN lattice are replaced by O atoms. Fig. 5(d) shows the O 1s spectra of bulk CN and CN-0.4. Both spectra can be deconvoluted into two peaks at 532.6 eV and 533.9 eV, which are attributed to the surface hydroxyl groups

and the intermediates of melamine thermal-polymerization, respectively [56]. However, another peak at 531.6 eV is obviously detected for the CN-0.4, which is attribute to the C-O species, indicating that oxygen has been doping in C₃N₄ [51,57]. After integration, the relative proportion of the peaks at 531.6 eV, 532.6 eV and

533.9 eV can be calculated of 49%, 42% and 9%, respectively. This phenomenon also corresponds to the FTIR and NMR characterizations. In addition, in order to accurately measure the ratio of the elements, the results from the CHNSO elemental analysis of CN and OCN nanotubes are provided, as shown in Table S3, which is s corresponding to XPS results.

Fig. 6 shows the photocatalytic performance of our samples under visible light illumination. It can be seen that bulk CN only exhibits a HER of about 11.84 µmol h⁻¹. All OCN samples exhibit the higher photocatalytic performance than that of bulk CN, indicating that the optimal nanostructure and oxygen doping can significantly improve the photocatalytic performance, which is in keeping with previous characterizations. Furthermore, it is noted that the HER of OCN increases with the increase of citric acid firstly, and then reaches a maximum value of $73.84 \text{ }\mu$ the CN-0.4, outperforming the HER performance of most of reported one dimensional (1D) g-C₃N₄ previously (details see in Table S4). This phenomenon is due to the optimization of nanostructure and oxygen doping, resulting in the increase of absorbance and separation of photogenerated carriers. With the further increase of citric acid (CN-0.6), the HER performance diminishes, indicating that excess citric acid can generate excess defect in g-C₃N₄, resulting the poor separating performance of photogenerated carriers. Furthermore, the SA of photocatalyst has a direct influence on active sites and the transfer efficiency of photogenerated carriers [5]. In order to investigate the effect of SA on the photocatalytic performance of bulk CN and various OCN samples, the normalized HER by SA (HER/SA) are calculated, as shown in Fig. S5. The HER/SA of OCN samples are still much larger than that of bulk CN, and CN-0.4 still has the largest HER/SA value among all samples.

In order to investigate the stability of our photocatalyst, the cyclic performance of HER for CN-0.4 is performed, as show in Fig. 6(b). In the initial cycle, the HER of the CN-0.4 is 295.36 μ mol after 4 h under visible light illumination. With the cycle proceeding, the HER maintains a retention rate of 99.1% in the second cycle and still remains highly stable after third cycle for CN-0.4. Furthermore, the HER of fresh samples and the samples stored for 6 months are also measured to access their storage stability, as shown in Fig. 6(c). It is found that the HER of CN-0.4 reveals no fade photocatalytic performance after storage of 6 months. The above results indicate that nanotubes structure and the oxygen-doping of CN-0.4 possesses excellent reusability and storage stability for photocatalytic water splitting for HER.

To assess the apparent quantum efficiency (AQE), the HER of CN-0.4 was measured under the illumination with a 420 nm 420, 435, 450, 470, 500, 520, and 550 nm cut-off filter, respectively (Fig. 6(d)). The AQE can be calculated according to the following formula (1) [58]:

$$AQE(\%) = 2 \times N_{H2}/N_e \times 100\%$$

where $N_{\rm H2}$ indicates the number of evolved H_2 molecules and $N_{\rm e}$ represents the number of incident photons. In Fig. 6(d), the solid line indicates the function of the wavelength and the point is the AQE's values of CN-0.4. The AQE of CN-0.4 under 420 nm, 435 nm and 450 nm light irradiation are 4.22%, 1.53% and 1.01%, respectively, indicating that H_2 evolution majorly arises under light illumination within 400~450 nm. It is noted that the AQE curve exhibits a consistency with the absorption spectrum of the CN-0.4, signifying that the HER is mainly driven by photo-excitation [50].

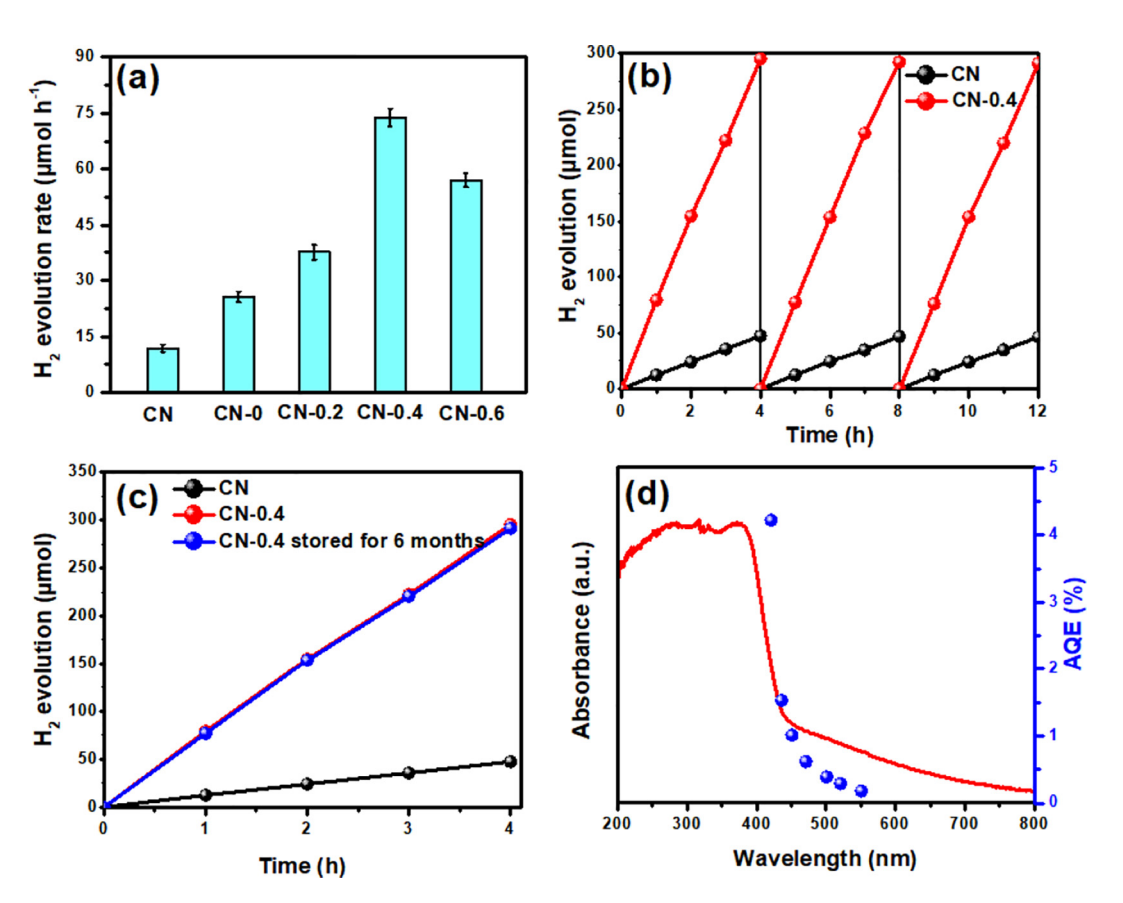


Fig. 6. (a) The HER of the bulk CN and OCN samples under visible-light irradiation; (b) stability cycles of the bulk CN and CN-0.4 nanotubes for H_2 evolution under visible-light irradiation; (c) the HER of fresh CN-0.4 and CN-0.4 after six months of storage compared with the bulk CN; (d) the wavelength dependent AQE of CN-0.4.

In order to further prove the structure stability of our OCN nanotubes after photocatalytic reaction, the XRD patterns and FTIR spectra of CN-0.4 before and after photocatalytic water splitting are provided, as shown in Fig. 7(a, b). Both results indicate that the crystal and chemical structures of CN-0.4 are almost unchanged before and after HER reaction, further demonstrating the incorruptibility and reusability of our OCN nanotubes.

To understand the photocatalytic effect of nanostructure and oxygen doping, the optical performances of bulk CN and OCN nanotubes are provided. Fig. 7(c) shows the photograph of bulk CN and OCN samples. It is found that the OCN samples gradually darken with the increase of citric acid in precursor compared to the yellow bulk CN, indicating that the absorbance of OCN nanotubes is increase. Fig. 7(d) shows the absorption spectra of bulk CN, the OCN samples. It is observed that the absorption edge of OCN samples exhibit red-shift apparently compared with bulk CN. Furthermore, the absorbance intensity of OCN samples also increases with the increase of citric acid during the range of 400-900 nm, which is consistent with the colour change in Fig. 7(c). To confirm the band gaps of bulk CN and the OCN samples, the plot of the Kubelka-Munk transformed function vs. photon energy are provided, as shown in Fig. 7(e). After linear fitting, the values of band gaps $(E_{\rm g})$ can be obtained and the corresponding values of $E_{\rm g}$ are 2.75, 2.70, 2.62, 2.52 and 2.49 eV for CN, CN-0, CN-0.2, CN-0.4, and CN-0.6, respectively. With the decrease of $E_{\rm g}$, OCN nanotubes can be easily excited by longer-wavelength of sunlight to generate photogenerated electrons and holes, enabling more efficient use of sunlight. Furthermore, all the OCN samples exhibit better absorbance compared with bulk CN in full-wavelength. This phenomenon should be attributed to the multiple reflections of incident light in the hollow nanotubes structure [59]. The corresponding multiple reflections schematic is shown in Fig. 7(f). Due to the multiple reflections, the absorbance of OCN nanotubes increased, which will remarkably promote the utilization of visible light.

In addition, the separation of photogenerated carriers is important parameter for photocatalysis. Fig. 7(g) shows the PL spectra of bulk CN and OCN samples. Generally, the PL signal majorly arising from the recombination of photogenerated carriers [37,60]. It is found that All OCN nanotubes exhibit lower PL intensity compared to bulk CN, indicating the lower recombination rate of photogener-

ated carriers after oxygen doping [47,51]. Furthermore, it is found that CN-0.4 exhibits the lowest PL intensity compared with other OCN samples, indicating that it possesses the highest separation efficiency of photogenerated carriers, which will significantly improve its photocatalytic performance. To further confirm the separating performance of photogenerated carriers for our samples, the photocurrent responses of bulk CN and OCN samples are operated, as shown in Fig. 7(h). It is found that the photocurrents of all samples are fast, coincident and repeatable. The order of photocurrent densities of all sample arranged in the following order: CN < CN-0 < CN-0.2 < CN-0.6 < CN-0.4. Such intensive photocurrent density of CN-0.4 indicates that CN-0.4 possesses the largest carrier mobility and minimum carrier recombination rate, which is in accord with the PL result [37,45]. Fig. 8(a) shows the EIS of bulk CN and OCN samples. It is observed that CN-0.4 exhibits the lowest arc radius, indicating that CN-0.4 exhibits a fast charge transfer rate. This result further testify the our OCN samples exhibit an improvement of charge transfer rate, which is beneficial for enhancing its photocatalytic performance [5,37,45].

It is well known that energy positions of the conduction band (CB) and valence band (VB) are directly related to oxidizing capacity and reducing capacity of g-C₃N₄, respectively [61]. Fig. 8(b) shows the energy positions of VB maximum of bulk CN and OCN nanotubes, which are determined by the VB spectra of XPS. The VB maximum value can be calculated of 1.58, 1.58, 1.56, 1.50 and 1.49 eV vs Vacuum for bulk CN, CN-0, CN-0.2, CN-0.4 and CN-0.6, respectively. Furthermore, the V_{fb} of bulk CN, CN-0, CN-0.2, CN-0.4 and CN-0.6 are determined to be -0.11 V, -0.07 V, -0.06 V, -0.04 V and 0.04 V vs AgCl, respectively according the Mott-Schottky plots in Fig. S7. Therefore, the VB value (E_{VB}) of bulk CN, CN-0, CN-0.2, CN-0.4 and CN-0.6 can be obtained of 1.47, 1.51, 1.50, 1.46 and 1.46 V vs AgCl, respectively. Previously, we have obtained the values of $E_{\rm g}$ of bulk CN and OCN nanotubes by optical performances. Therefore, the energy positions of conduction band minimum (E_{CB}) can be obtained as the follow formula:

$$E_{\rm CB} = E_{
m VB} - E_{
m g}$$

After the confirmation of the position of $E_{\rm CB}$ and $E_{\rm VB}$, the corresponding band structure schematic of bulk CN and OCN nanotubes can be obtained, as shown in Fig. 8(c). It can be seen that the $E_{\rm CB}$ of OCN shifts downward from -1.28 V vs AgCl for bulk CN to -1.03 V

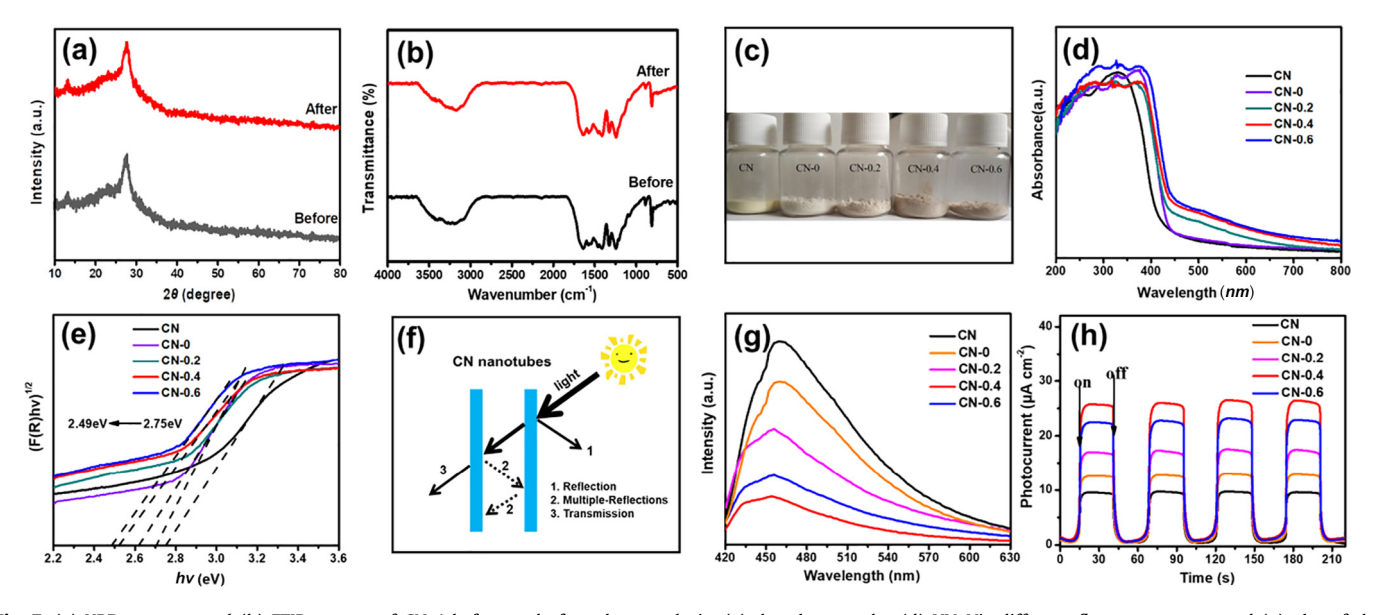


Fig. 7. (a) XRD patterns and (b) FTIR spectra of CN-4 before and after photocatalysis; (c) the photographs, (d) UV–Vis diffuse reflectance spectra and (e) plot of the transformed Kubelka-Munk function (F(R1)) versus the photon energy (hv) for the bulk CN and OCN samples; (f) multiple diffuse reflection schematic of nanotubes; (g) PL spectra and (h) photocurrent responses of the bulk CN and OCN samples.

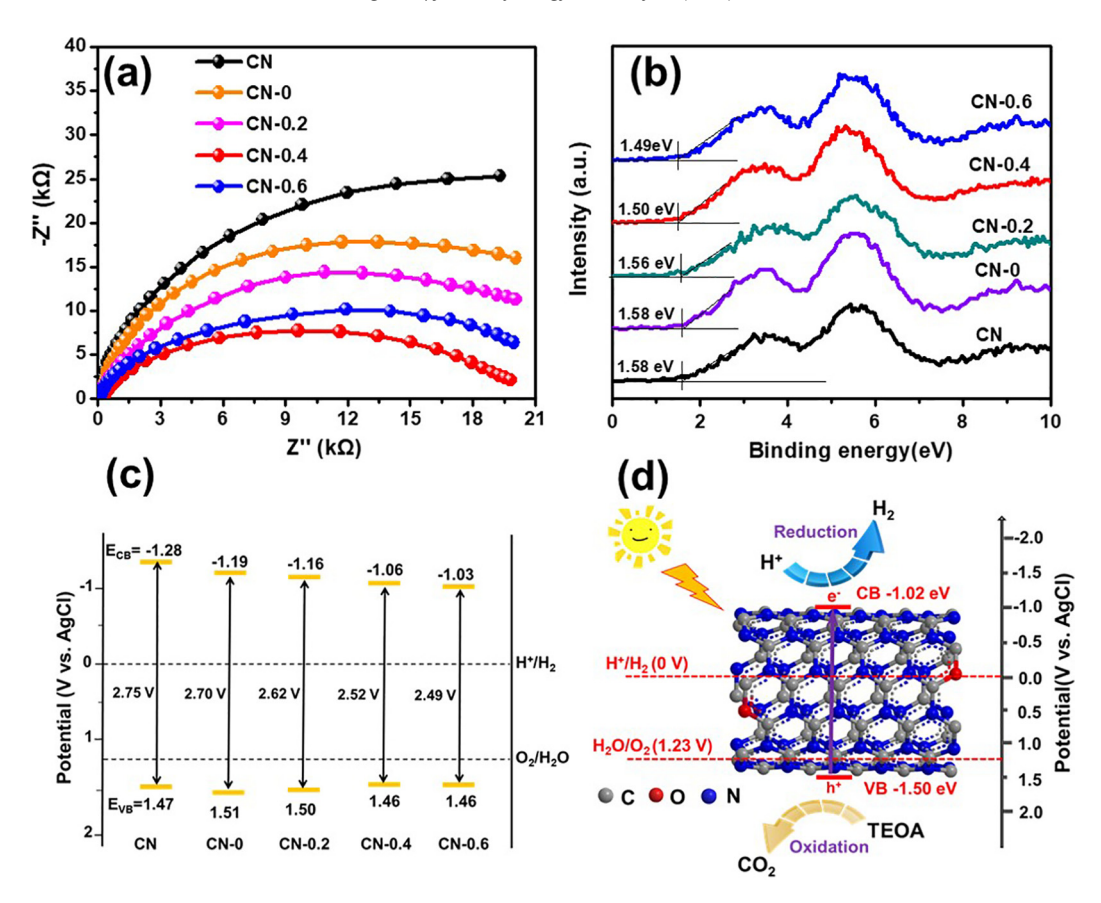


Fig. 8. (a) EIS of CN and OCN samples after the buildup on the ITO electrodes under visible-light irradiation; (b) XPS VB spectra and (c) band structure alignments of CN and OCN samples; (d) photocatalytic hydrogen evolution schematic of OCN nanotubes.

vs AgCl for CN-0.6. Therefore, the upward shift of VB and downward shift of CB together can lead to band gap narrowing of the OCN, which is accordance with previously reported by Liu' group [60]. Unquestionable, lower CB energy position should lead to smaller reducing capacity.

According to above analysis, the improvement mechanism for photocatalytic performance of OCN photocatalyst is proposed on the basis of synergistic effect of nanotube structure and oxygen doping, as shown in Fig. 8(d). Due to the nanotube structure, our OCN possess many unique advantages in photocatalytic water splitting, including higher visible light absorption and scattering, faster electron transport rate, larger number of active centers, larger specific surface area, and higher photogenerated carriers' separation rate, which have been proven by our previous characterization [17,18,57]. Furthermore, we also demonstrate that the oxygen atoms have been doped into our OCN samples, which will significantly affect the photocatalytic performance. With the doping of oxygen, the intermediate state can serve as active sites for photogenerated carriers' excitation, and cause band gap narrowing, resulting the expansion of photo response range of OCN nanotubes [51]. Meanwhile, the doping of oxygen in OCN can improve the photogenerated carriers' separation efficiency, consequently enlarging overall quantum efficiency [51]. However, the upward shift of VB as well as the downward shift of CB can be detected after oxygen doping, which can reduce the redox ability of the of OCN nanotubes. Among in above features, the expansion of photo response range and improvement of the photogenerated carriers' separation efficiency are beneficial for improving photocatalytic performance of OCN nanotubes. However, feature of the VB's upward shift and the CB's downward shift is unbeneficial because the smaller the energy level gap between the band positions of semiconductor catalyst and redox agent, the smaller the transfer rate between the photo-generated carriers in catalyst and the reactants [60,62]. An optimal oxygen doping concentration can attain the highest HER performance for the sample.

4. Conclusions

In this work, we obtained OCN nanotubes derived by rod-like supramolecular intermediate, which prepared through molecular self-assembly under citric acid-assisted hydrothermal condition. Compare to bulk CN, our OCN nanotubes exhibit tremendous improvement of light absorption as well as visible-light photocatalytic performance. The optimal OCN nanotubes photocatalyst exhibits remarkable HER of 73.84 µmol h⁻¹, which is 6.24 times of bulk CN. The enhanced photocatalytic performance of OCN nanotubes should be ascribed to unique advantages induced by synergetic effect of nanotubes structure and oxygen doping, including the higher visible light absorption and scattering, faster electron transport rate, larger number of active centres, larger specific surface area, and higher photogenerated carrier separation rate. This work provides a convenient strategy for preparing polymer precursors by molecular self-assembly technology and further designing high activity photocatalysts with controllable nanostructures. It is hoped that this work can facilitate the promotion of technology of supermolecular intermediates as precursors to synthesize high performance g-C₃N₄ photocatalysts.

Declaration of Competing Interest

The authors declare that they have no known competing financial interests or personal relationships that could have appeared to influence the work reported in this paper.

Acknowledgments

This work was financially supported by the Key-Area Research Development Program of Guangdong (2019B010937001), the National Natural Science Foundation of China (50702022, 51577070, 51702056 and U1601208), Natural Science Foundation of Guangdong Province (2019A1515012129), Science and Technology Planning Project of Guangdong Province (2016B090932005).

Appendix A. Supplementary data

Supplementary data to this article can be found online at https://doi.org/10.1016/j.jechem.2020.05.043.

References

- [1] X.P. Tao, Y. Zhao, L.C. Mu, S.Y. Wang, R.G. Li, C. Li, Adv. Energy Mater. 8 (1) (2018) 1701392.
- [2] X.X. Hong, J. Tan, H.Z. Zhu, N.D. Feng, Y.Q. Yang, J.T.S. Irvine, L.Z. Wang, G. Liu, H.M. Cheng, Chem. Eur. J. 25 (7) (2019) 1787–1794.
- [3] M.S. Zhu, Z.C. Sun, M. Fujitsuka, T. Majima, Angew. Chem. Int. Ed. 57 (8) (2018) 2160-2164.
- [4] W.J. Ong, L.L. Tan, Y.H. Ng, S.T. Yong, S.P. Chai, Chem. Rev. 116 (12) (2016) 7159-7329.
- [5] Z. Chen, H. Jiang, W. Jin, C. Shi, Appl. Catal. B-Environ. 180 (2016) 698-706.
- [6] A. Mishra, A. Mehta, S. Basu, N.P. Shetti, K.R. Reddy, T.M. Aminabhavi, Carbon 149 (2019) 693-721.
- [7] L.Q. Kong, Y.J. Ji, Z.Z. Dang, J.Q. Yan, P. Li, Y.Y. Li, S.Z. Liu, Adv. Funct. Mater. 28 (22) (2018) 1800668.
- [8] J.W. Fu, J.G. Yu, C.J. Jiang, B. Cheng, Adv. Energy Mater. 8 (3) (2018) 1701503. [9] W. Zhou, T. Jia, H.X. Shi, D.S. Yu, W. Hong, X.D. Chen, J. Mater. Chem. A 7 (1)
- (2019) 303-311.
- [10] X.C. Wang, K. Maeda, A. Thomas, K. Takanabe, G. Xin, J.M. Carlsson, K. Domen, M. Antonietti, Nat. Mater. 8 (1) (2009) 76–80.
- [11] H. Xu, J. Yi, X. She, Q. Liu, L. Song, S. Chen, Y. Yang, Y. Song, R. Vajtai, J. Lou, H. Li, S. Yuan, J. Wu, P.M. Ajayan, Appl. Catal. B-Environm. 220 (2018) 379–385.
- [12] V.W.-H. Lau, M.B. Mesch, V. Duppel, V. Blum, J. Senker, B.V. Lotsch, J. Am. Chem. Soc. 137 (3) (2015) 1064–1072.
- [13] S. Cao, J. Low, J. Yu, M. Jaroniec, Adv. Mater. 27 (13) (2015) 2150–2176.
 [14] S. Zhang, P.C. Gu, R. Ma, C.T. Luo, T. Wen, G.X. Zhao, W.C. Cheng, X.K. Wang, Catal. Today 335 (2019) 65–77. [15] S.N. Talapaneni, G. Singh, I.Y. Kim, K. AlBahily, A.H. Al-Muhtaseb, A.S. Karakoti,
- E. Tavakkoli, A. Vinu, Adv. Mater. 32 (18) (2019) 1904635. [16] S.F. Kang, M.F. He, M.Y. Chen, Z.G. Wang, Z.Z. Sun, H.F. Dang, X.J. Chang, M.D.
- Dong, P. Liu, L.F. Cui, J. Colloid Interf. Sci. 556 (2019) 214-223.
- [17] K. Zhang, L. Wang, X. Sheng, M. Ma, M.S. Jung, W. Kim, H. Lee, J.H. Park, Adv. Energy Mater. 6 (11) (2016) 1502352.
- [18] H.J. Li, D.J. Qian, M. Chen, ACS Appl. Mater. Interfaces 7 (45) (2015) 25162-25170
- [19] S. Obregon, A. Vazquez, M.A. Ruiz-Gomez, V. Rodriguez-Gonzalez, Appl. Surf. Sci. 488 (2019) 205-212.
- [20] W. Iqbal, B. Yang, X. Zhao, M. Waqas, M. Ranf, C.Q. Guo, J.L. Zhang, Y.P. Mao, Appl. Catal. A-Gen. 573 (2019) 13-21.
- [21] N.A. Wasio, R.C. Quardokus, R.P. Forrest, C.S. Lent, S.A. Corcelli, J.A. Christie, K.
- W. Henderson, S.A. Kandel, Nature 507 (2014) 86-89. [22] M. Shalom, M. Guttentag, C. Fettkenhauer, S. Inal, D. Neher, A. Llobet, M.
- Antonietti, Chem. Mater. 26 (19) (2014) 5812-5818. [23] T. Jordan, N. Fechler, J.S. Xu, T.J.K. Brenner, M. Antonietti, M. Shalom, ChemCatChem 7 (18) (2015) 2826-2830.
- [24] M. Shalom, S. Inal, C. Fettkenhauer, D. Neher, M. Antonietti, J. Am. Chem. Soc. 135 (19) (2013) 7118–7121.
- [25] Y.S. Jun, J. Park, S.U. Lee, A. Thomas, W.H. Hong, G.D. Stucky, Angew. Chem. Int. Ed. 52 (42) (2013) 11083-11087.

- [26] K. Jutzi, A.M. Cook, R. Hütter, Biochem. J. 208 (3) (1982) 679-684.
- [27] Y.Y. Huang, D. Li, Z.Y. Fang, R.J. Chen, B.F. Luo, W.D. Shi, Appl. Catal. B-Environ. 254 (2019) 128-134.
- [28] X. Yu, X.L. Fan, L. An, G.B. Liu, Z.H. Li, J.W. Liu, P.A. Hu, Carbon 128 (2018) 21-
- [29] B. Wang, H.R. Cai, D.M. Zhao, M. Song, P.H. Guo, S.H. Shen, D.S. Li, S.C. Yang, Appl. Catal. B-Environ. 244 (2019) 486-493.
- [30] A. Kharlamov, M. Bondarenko, G. Kharlamova, N. Gubareni, Diam. Relat. Mater. 66 (2016) 16-22.
- [31] P.X. Qiu, C.M. Xu, H. Chen, F. Jiang, X. Wang, R.F. Lu, X.R. Zhang, Appl. Catal. B-Environm. 206 (2017) 319-327.
- [32] F.Y. Wei, Y. Liu, H. Zhao, X.N. Ren, J. Liu, T. Hasan, L.H. Chen, Y. Li, B.L. Su, Nanoscale 10 (2018) 4515-4522
- [33] J.H. Li, B.A. Shen, Z.H. Hong, B.Z. Lin, B.F. Gao, Y.L. Chen, Chem. Commun. 48 (98) (2012) 12017–12019.
- [34] Y.X. Zeng, X. Liu, C.B. Liu, L.L. Wang, Y.C. Xia, S.Q. Zhang, S.L. Luo, Y. Pei, Appl. Catal. B-Environm. 224 (2018) 1-9.
- [35] C.Y. Liu, H.W. Huang, W. Cui, F. Dong, Y.H. Zhang, Appl. Catal. B-Environm. 230 (2018) 115-124.
- [36] L.J. Fang, X.L. Wang, J.J. Zhao, Y.H. Li, Y.L. Wang, X.L. Du, Z.F. He, H.D. Zeng, H.G. Yang, Chem. Commun. 52 (100) (2016) 14408-14411.
- [37] S. Guo, Z. Deng, M. Li, B. Jiang, C. Tian, Q. Pan, H. Fu, Angew. Chem. Int. Ed. 55 (5) (2016) 1830–1834.
- [38] S. Lu, C. Li, H.H. Li, Y.F. Zhao, Y.Y. Gong, L.Y. Niu, X.J. Liu, T. Wang, Appl. Surf. Sci. 392 (2017) 966-974.
- [39] M. Prabhaharan, A.R. Prabakaran, S. Srinivasan, S. Gunasekaran, Spectrochim. Acta. A 138 (2015) 711-722.
- [40] Y.S. Jun, E.Z. Lee, X.C. Wang, W.H. Hong, G.D. Stucky, A. Thomas, Adv. Funct. Mater. 23 (29) (2013) 3661-3667.
- [41] G. Arrachart, C. Carcel, P. Trens, J.J. Moreau, M. Wong Chi Man, Chem. Eur. J. 15 (25) (2009) 6279-6288.
- [42] J. Gao, Y. Zhou, Z.S. Li, S.C. Yan, N.Y. Wang, Z.G. Zou, Nanoscale 4 (12) (2012) 3687-3692.
- [43] H. Pan, Y.W. Zhang, V.B. Shenoy, H.J. Gao, ACS Catal. 1 (2) (2011) 99-104.
- [44] Z. Pan, Y. Zheng, F. Guo, P. Niu, X. Wang, ChemSusChem 10 (1) (2017) 87-90.
- [45] Y. Zhang, J. Gao, Z. Chen, J. Colloid Interf. Sci. 535 (2019) 331-340.
- [46] P. Niu, L.L. Zhang, G. Liu, H.M. Cheng, Adv. Funct. Mater. 22 (22) (2012) 4763-
- [47] Q. Han, B. Wang, Y. Zhao, C.G. Hu, L.T. Qu, Angew. Chem. Int. Ed. 54 (39) (2015) 11433-11437.
- [48] L.S. Zhang, N. Ding, J.H. Wu, K.D. Iwasaki, L.H. Lin, Y.C. Yamaguchi, Y.K. Shibayama, J.J. Shi, H.J. Wu, Y.H. Luo, K. Nakata, D.M. Li, X.C. Wang, A. Fujishima, Q.B. Meng, Catal. Sci. Technol. 8 (15) (2018) 3846-3852.
- [49] P. Niu, M. Qiao, Y.F. Li, L. Huang, T.Y. Zhai, Nano Energy 44 (2018) 73-81.
- [50] J.S. Zhang, M.W. Zhang, C. Yang, X.C. Wang, Adv. Mater. 26 (24) (2014) 4121-
- [51] G.Z. Liao, S. Chen, X. Quan, H.T. Yu, H.M. Zhao, J. Mater. Chem. 22 (6) (2012) 2721-2726.
- [52] H.J. Yu, R. Shi, Y.X. Zhao, T. Bian, Y.F. Zhao, C. Zhou, G.I.N. Waterhouse, L.Z. Wu, C.H. Tung, T.R. Zhang, Adv. Mater. 29 (16) (2017) 1605148.
- [53] J.X. Huang, D.G. Li, R.B. Li, Q.X. Zhang, T.S. Chen, H.J. Liu, Y. Liu, W.Y. Lv, G.G. Liu, Chem. Eng. J. 374 (2019) 242–253.
- [54] J. Wei, P. Hing, Z.Q. Mo, Surf. Interface Anal. 28 (1) (1999) 208-211.
- [55] P.J. Yang, H.H. Ou, Y.X. Fang, X.C. Wang, Angew. Chem. Int. Ed. 56 (14) (2017) 3992-3996.
- [56] L.N. Bùi, M. Thompson, N.B. McKeown, A.D. Romaschin, P.G. Kalman, Analyst 118 (5) (1993) 463-474.
- [57] J. Fu, B. Zhu, C. Jiang, B. Cheng, W. You, J. Yu, Small 13 (15) (2017) 1603938.
- [58] W.G. Tu, Y. Xu, J.J. Wang, B.W. Zhang, T.H. Zhou, S.M. Yin, S.Y. Wu, C.M. Li, Y.Z. Huang, Y. Zhou, Z.G. Zou, J. Robertson, M. Kraft, R. Xu, ACS Sustain. Chem. Eng. 5 (8) (2017) 7260-7268.
- [59] X.C. Wang, K. Maeda, X.F. Chen, K. Takanabe, K. Domen, Y.D. Hou, X.Z. Fu, M. Antonietti, J. Am. Chem. Soc. 131 (5) (2009) 1680-1681.
- [60] P. Niu, L.C. Yin, Y.Q. Yang, G. Liu, H.M. Cheng, Adv. Mater. 26 (47) (2014) 8046-8052.
- [61] B. Wang, J. Di, P.F. Zhang, J. Xia, S. Dai, H.M. Li, Appl. Catal. B-Environ. 206 (2017) 127–135.
- [62] O. Pliekhova, O. Pliekhov, M. Fanetti, I. Arcon, N.N. Tusar, U.L. Stangar, Catal. Today 328 (2019) 105-110.